Research Article | Vol. 31, No. 20 / 25 Sep 2023 / Optics Express 33449
Optics EXPRESS

# Vertical-cavity surface-emitting phase shifter

DHAIFALLAH ALMUTAIRI,[1,2,*] KARL JOHNSON,[1] ALEXEI SMOLYANINOV,[1] ANDREW GRIECO,[3] AND YESHAIAHU FAINMAN[1]

[1]Department of Electrical and Computer Engineering, University of California, San Diego, California 92093, USA
[2]King Abdulaziz City for Science and Technology (KACST), Riyadh cisc11442, Saudi Arabia
[3]Qualcomm Institute, University of California, San Diego, California 92093, USA
[*]Daalmuta@eng.ucsd.edu

**Abstract:** This study proposes a novel technique for a 2D beam steering system using hybrid plasmonic phase shifters with a cylindrical configuration in a 2D periodic array suitable for LIDAR applications. A nanoscale VCSEP design facilitates a sub-wavelength spacing between individual phase shifters, yielding an expanded field of view and side lobes suppression. The proposed design includes a highly doped sub-micron silicon pillar covered by a thin layer of nonlinear material and an additional conductive metal layer. Characterization of a single VCSEP demonstrated a Free Spectral Range (FSR) of $53.28 \pm 2.5$ nm and a transmission variation of 3 dB, with $V_\pi L$ equal to 0.075 V-mm.



## 1. Introduction

Optical beam steering is an important technology utilized by many applications, including optical wireless communication systems [1], LiDAR systems [2], remote sensing [3], and medical imaging [4]. Phased arrays represent the most advanced beam steering technique, widely used in radio frequency (RF) systems. The primary drawback of this approach is the unfavorable manner in which the emitter array spacing scales with wavelength. This poses formidable fabrication challenges at optical and infrared frequencies. For example, achieving a 110° steering angle for a 1550 nm wavelength beam requires an array period of around 0.5 $\mu m^2$ [5,6].

State-of-the-art chip-scale phased array optics have been implemented using 2D phase shifter arrays based on waveguide-coupled directional gratings [7]. These devices employ an architecture where photonic waveguides supply a linear array of add/drop filters. The coupling into each add/drop filter can be modulated thermally using metal heaters. Following the add/drop process, light is transmitted to grating nanoantennas, which emit the light vertically. Compact $64 \times 64$ phase shifter arrays with a pixel size of 9 µm x 9 µm or 89 $\mu m^2$ have been reported [7]. However, such approaches are inherently limited in pixel size by the waveguide couplers themselves, which, due to the physical requirements of wavelength scaling, must be longer than 1 µm, as observed in [7].

This paper presents an innovative method for designing optical phase shifters using hybrid plasmonic phase shifters in a cylindrical configuration. This approach holds significant potential for constructing large-scale 2D optical phase shifter arrays with sub-wavelength spacing. Furthermore, we provide an in-depth analysis of the proposed optical phaser shifter design, fabrication, and characterization.

## 2. Approach description

Our proposed approach involves the utilization of the hybrid plasmonic phase shifter in cylindrical geometry to construct a hybrid plasmonic resonator called a Vertical Cavity Surface Emitting Plasmonic (VCSEP) device, shown schematically in Fig. 1. The optical input beam is introduced via an integrated bottom layer into the VCSEP device, which modulates this optical carrier.

#497606 https://doi.org/10.1364/OE.497606
Journal © 2023 Received 8 Jun 2023; revised 27 Aug 2023; accepted 11 Sep 2023; published 21 Sep 2023

Optics EXPRESS

The modulated field is re-emitted vertically through the top of the device. As the input light traverses the VCSEP device, it is converted into a localized hybrid plasmonic mode in a resonant configuration, modulated in the nonlinear optical material by the voltage applied across it, and subsequently emitted from the output of the device. The fusion of localization and resonance effects significantly augments the effective interaction length. A voltage is applied to the metal shell through a metal contact. At the same time, a doped silicon core connected to a doped silicon substrate serves as the ground electrode. This induces an electric field within the nonlinear electro-optic material inside the VCSEP, consequently modulating the refractive index within an individual VCSEP element. The synergy of enhanced effective interaction length and modulating refractive index within the cavity facilitates a phase shift. The light is then re-emitted into free space.

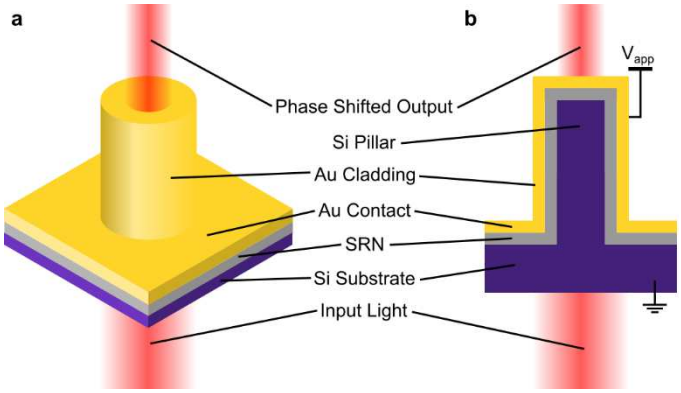


**Fig. 1.** A schematic diagram for the proposed Vertical Cavity Surface Emitting Phase shifter (VCSEP) illustrates its operating principle in the transmission mode. Light enters through the bottom of the device, undergoes a phase shift, and exits from the top side. (a) The VCSEP structure comprises a highly doped silicon core coated with a thin nonlinear dielectric core, specifically Silicon Rich Nitride (SRN), covered with a thin layer of gold. (b) A cross-section view of the VCSEP device provides a more detailed view of the device structure. This view highlights using gold as an electrical connection, allowing for applying an electrical field across the nonlinear material. The gold layer can be utilized for electrical connection to apply an electrical field across the nonlinear material. The substrate is utilized as a ground due to the high doping concentrations.

VCSEP devices exploit hybrid plasmonic localization to amplify the effective interaction length of light with the nonlinear material present within the resonant cavity [8–10]. Due to plasmonic effects in the vertical architecture, the enhancement in interaction length results in more pronounced phase shifts. Reduced loss can be achieved while maintaining high localization due to the overlap between photonic and plasmonic modes. Moreover, the impedance mismatch between the vertical hybrid plasmonic waveguide and free space generates a low finesse, low-quality factor (Q) cavity resonator.

Utilizing a low-Q cavity mitigates the traditional bandwidth and spectral range constraints typically encountered in high-Q photonic resonator-based modulators while benefiting from an interaction length increase due to a cavity finesse ranging from 10 to 20. This effect is further amplified by large k-vector plasmonic modes that exhibit spatial localization: hybrid plasmonic modes excited by a free space 1550 nm laser will possess an effective wavelength up to 20 times shorter within the hybrid plasmonic structure [8,9].

Optics EXPRESS

## 3. Design and simulations

The versatility of the hybrid plasmonic design facilitates optimization for either low loss (less than 1000 dB/cm) or high localization, contingent on the radii of the Si core, the interstitial layer of nonlinear dielectric, and the metal shell. In the case of a small Si core, the photonic mode is compelled into the nonlinear dielectric between the metal and Si core, resulting in enhanced interaction with the nonlinear dielectric while maintaining some plasmonic localization (as shown in the left panel of Fig. 2). Alternatively, the electromagnetic field is effectively confined within the nonlinear dielectric with a thick Si core and substantial metal cladding. It exhibits strong localization in a thin section of the nonlinear dielectric at the cost of increased loss. The mode profile is determined by Maxwell's equations applied to the boundary conditions formed by the waveguide materials. For the geometry of the materials in Fig. 2 the fundamental TE and TM modes are degenerate, and have the profiles that are illustrated in the figure below.

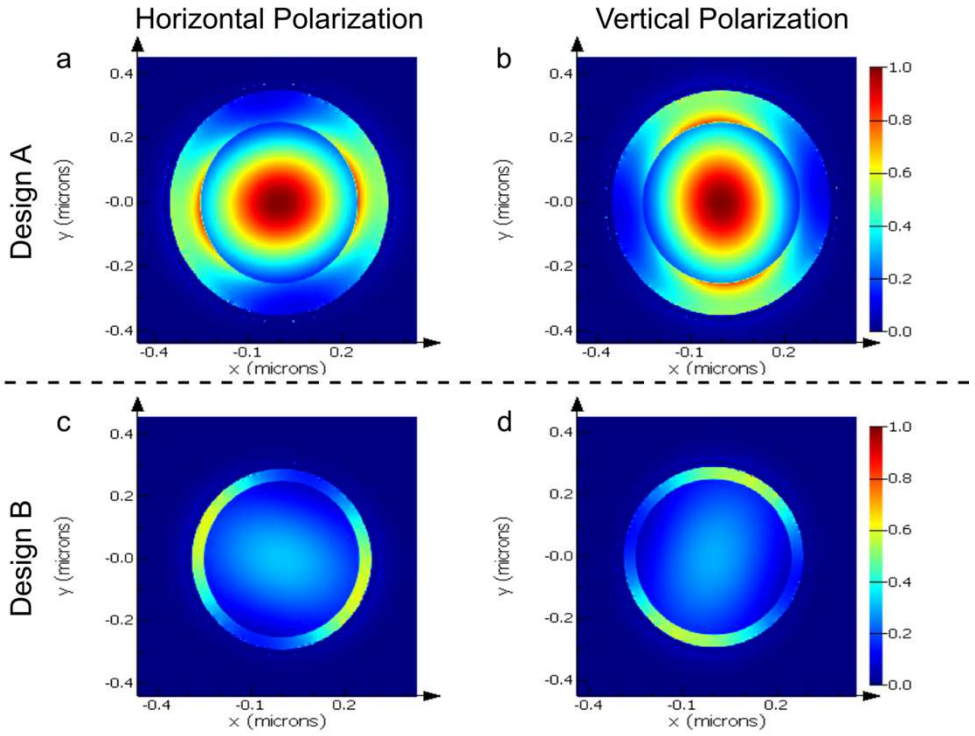


**Fig. 2.** Representation of two possible configurations for a vertical-cavity surface-emitting plasmon (VCSEP) and their corresponding normalized electric field (E-field) localization. The first configuration (a and b) depicts the normalized E-field obtained from a Lumerical simulation of a VCSEP with a core radius of 250 nm, coated with 100 nm of silicon-rich nitride (SRN), and finally sputtered with 20 nm of metal. The E-field is shown for both horizontal (a) and vertical (b) polarizations. The second configuration (c and d) shows the normalized E-field obtained from a Lumerical simulation of a VCSEP with a core radius of 250 nm, coated with 40 nm of SRN, and finally sputtered with 10 nm of metal. The E-field is shown for both horizontal (c) and vertical (d) polarizations.

We utilized Lumerical mode solver simulations to create two VCSEP designs. The initial design (A) comprises a Si core with a thickness of 500 nm, a cladding of SRN with a thickness of 100 nm, and an additional layer of Au with a thickness of 20 nm. In design (A) the hybrid plasmonic mode is more confined to the low-loss materials and depending on the precise geometry chosen can

Optics EXPRESS

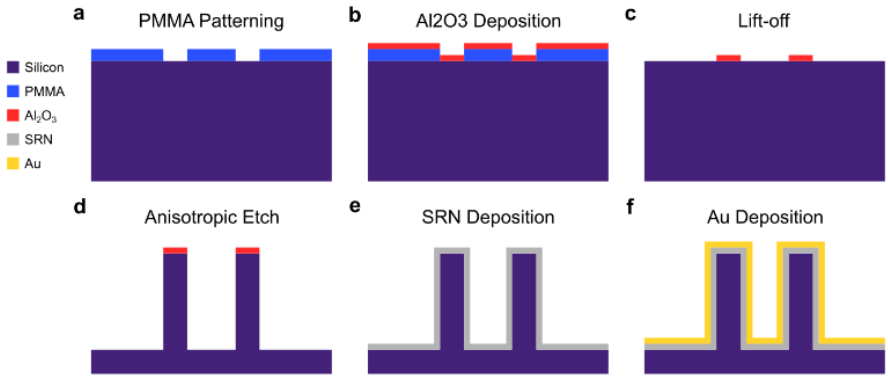


**Fig. 3.** The figure depicts the fabrication process of VCSEP and the steps involved in it. The process includes the following stages: (a) Spreading a 500 nm layer of PMMA using the spin-coating technique and transferring the pattern with E-beam, (b) Applying a layer of AL2O3 to act as a hard mask, (c) Removing the PMMA layer through lift-off, (d) Etching the pillars to a high aspect ratio and then removing the hard mask, (e) Coating the pillars with SRN, a nonlinear material, through PECVD method, and (f) Adding a thin layer of gold to the pillars.

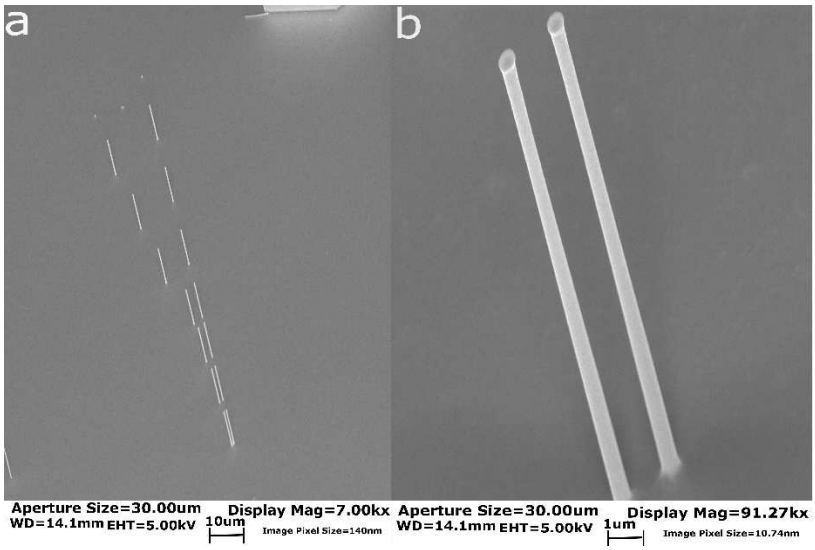


**Fig. 4.** SEM image of the VCSEP pillars after undergoing high aspect ratio etching. The image comprises two parts: (a) an SEM overview image of the VCSEP structure, which has a height of 7.403 µm, a width of 500 nm, and a separation gap ranging from 13 µm to 500 nm. (b) a zoomed-in SEM image showcases a pillar with an aspect ratio of 15 and a separation gap of 0.5 µm.

have a lower propagation loss value on the order of ~1000 dB/cm. This configuration is optimized for the high nonlinear coefficient by leveraging a good mode overlap between the EO material and the photonic mode, as shown in Fig. 2(a) and Fig. 2(b). A second VCSEP configuration (B) comprises a Si core with a thickness of 500 nm, a cladding of SRN with a thickness of 40 nm, and an additional layer of Au with a thickness of 20 nm. Design (B) relies on greater plasmonic localization can be obtained by reducing the thickness of the dielectric. Depending on the

Optics EXPRESS

precise geometry this type of device has a higher loss on the order of ~10000 dB/cm, as shown in Fig. 2(c) and Fig. 2(d). This configuration has higher plasmonic localization for a material platform with weaker nonlinear coefficients. Although the linear loss coefficient is relatively high for both options, it is important to note that the length of the VCSEP is approximately 7 μm, resulting in calculated insertion losses on the order of 3 dB and 10 dB for configurations A and B, respectively.

The oval shape of the mode is due to the superposition of degenerate TE and TM modes. The vertical polarization in Figs. 2(a) and 2(c) is dominated by degenerate TE modes, while the horizontal polarization in Figs. 2(b) and 2(d) is dominated by degenerate TM modes. The specific degenerate modes that are supported in this circular configuration of VCSEP.

Silicon Rich Nitride (SRN) as a nonlinear material provides an optimal material since the material index often combines second and third-order nonlinear susceptibility contributions; this is due to the contribution of Pockets and DC-Kerr effects, respectively [11]. Moreover, SRN has lower optical loss and higher breaking voltage [12,13] The utilized SRN has been characterized to have $\chi(2)$ of 22.7 pm/V at a refractive index of 2.25 [14].

## 4. Fabrication process

The sample substrate is a highly n-doped silicon wafer with a doping concentration of $4.5 \times 10^{18}\,\mathrm{cm}^{-1}$. The sample is first spin-coated utilizing polymethyl methacrylate (PMMA), achieving a thickness of 500 nm. Subsequently, a pattern was transferred to the sample via Vistec EBPG 5200 electron-beam lithography using a 1500 $\mu C/cm^2$ dosage. The pattern encompassed diverse circle diameters, ranging from 500 to 300 nm. The separation distances between each VCSEP varied from 0.5 μm to 13 μm (Fig. 3).

A layer of aluminum oxide ($Al_2O_3$) was deposited onto the transferred pattern through sputtering, serving as a hard mask. Previous studies have demonstrated that $Al_2O_3$ exhibits a selectivity of 70,000:1 with respect to silicon [15], making it an optimal choice for sensitive fabrication processes such as VCSEP. A 5 nm $Al_2O_3$ layer was radio-frequency (RF) sputtered using the Denton Discovery 635 Sputter System. The chamber pressure was maintained at 3.18 mTorr, while the RF power was set at 400 W. The lift-off process was subsequently performed to remove the excess resistance.

Single-step deep reactive ion etching (SDRIE) was performed using the Oxford Plasma 100 system, employing a highly controlled etching recipe that ensured smooth walls and a high etching rate (200 nm/min). The etching of the VCSEP pillars was executed via a combination of sulfur hexafluoride ($SF_6$) and argon (Ar) plasma, supplemented with octafluorocyclobutane ($C_4F_8$) to protect the pillar sidewalls through the deposition of an organic polymer. The flow rates of $SF_6$ and $C_4F_8$ were maintained at 28 sccm and 52 sccm, respectively. The chamber pressure was held constant at 19 mTorr during the etching procedure. The reactive ion etching (RIE) and inductively coupled plasma (ICP) generated power were set at 9 W and 850 W, respectively [16].

The height of each pillar is 7.403 μm, exhibiting an aspect ratio of 15. The hard mask was removed via chemical etching, primarily utilizing buffered oxide etching (BOE) for 10 seconds at an etching rate of 1 nm/sec. To ensure complete removal of the polymer, the sample was cleaned with a piranha solution (a mixture of $H_2SO_4$:$H_2O_2$ in a 3:1 ratio) at a temperature of 80°C.

Subsequently, Plasma Enhanced Chemical Vapor Deposition (PECVD) was employed to coat the VCSEP pillars with SRN. The chamber pressure was maintained at 15 mTorr, and the radio-frequency (RF) power was set at 50 W. The SRN deposition involved a combination of silane ($SiH_4$) and ammonia ($NH_3$).SRN has been shown to demonstrate a second-order nonlinear susceptibility $\chi^{(2)}$ equal to 22.7 pm/V at a refractive index of 2.25 [14].In the final step, the pillars were coated with a thin layer of gold utilizing the Denton 635 Sputter System. During the sputtering process, the chamber pressure was constant at 2.88 mTorr. Direct current (DC)

Optics EXPRESS

plasma power was set at 200 W for 55 seconds, giving a gold layer thickness of 60 nm and a rotated rate of 10 rpm (Fig. 4).

## 5. Characterization

The experimental setup shown in Fig. 5 was used to characterize the VCSEP. The laser source (Agilent model 81980A) was connected to a single-mode fiber (SMF) and then collimated using a fiber collimator (FC) before transmitting light through the backend of the sample. A 0.5 NA microscope objective (50X Mitutoyo Plan Apo NIR) was used to gather the transmitted light, which was then imaged onto the camera through a magnification setup consisting of a series of lenses acting as two sequential telescopes with a total magnification of 100. The camera used featured a pixel size of 25 µm by 25 µm. Once the VCSEP device was located, the removable mirror was taken off (as shown in Fig. 5) to collect the transmitted optical signal using a fiber collimated (FC) into a multimode fiber (MMF), which was then connected to a photodetector.

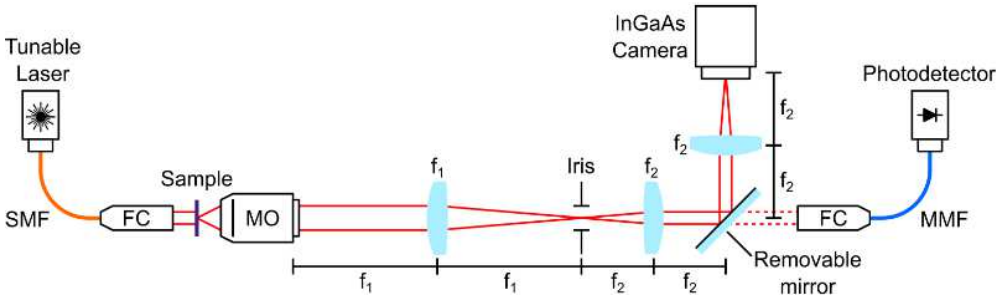


**Fig. 5.** Illustration of the experimental setup used to characterize the VCSEP. The setup includes a tunable laser connected to a Fiber Collimator (FC) through a Single Mode Fiber (SMF) to illuminate the backend of the sample. The transmitted light passes through a folded microscope setup composed of a 50X Mitutoyo Plan Apo NIR microscope objective (MO) and re-imaging lenses $f_1 = 40$ cm and $f_2 = 10$ cm. An iris is placed in an intermediate image plane to filter the system's field of view spatially. With the removable mirror in place, the final lens $f_2$ images collected light onto the IR camera, with a total system magnification of 100. Without the mirror, the light is directed to a photodetector using a fiber collimator and Multimode Fiber (MMF).

Characterizing a single VCSEP device poses challenges primarily due to its sub-micrometer diameter (~ 0.5 µm), making accurate structure identification difficult. To streamline the characterization process, large alignment marks are employed. This is illustrated in Fig. 6, where the SEM images of the single VCSEP are positioned at the center of the alignment marks, as shown in Fig. 6(a). Additionally, Fig. 6(b) displays an optical image captured from the IR camera at the end of the optical setup depicted in Fig. 5.

An iris was incorporated in the optical setup's first image plane to isolate a single VCSEP structure. This spatial filter limited any undesirable noise that could potentially impact device measurements. Fig. 5(c) illustrates the optical image detected by the IR camera after employing the iris to confine the illuminated area as closely as possible to the VCSEP illuminated region with a diameter smaller than 1 mm.

Optics EXPRESS

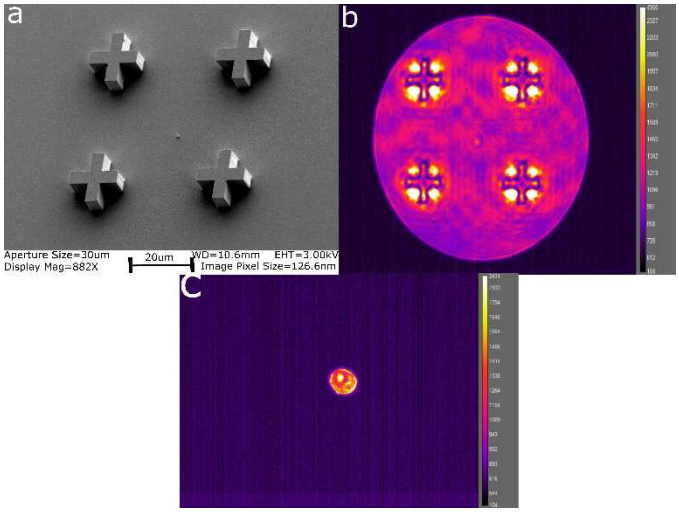


**Fig. 6.** The figure shows an improved VCSEP design incorporating an alignment mark to identify the device during imaging easily. The figure is composed of three parts: (a) an SEM image of the VCSEP device with an aspect ratio of 15 and height of 7.403 µm, which is surrounded by larger alignment marks to aid identification in an optical microscope, (b) an optical image captured by an IR camera that demonstrates optical transmission, and (c) an optical image captured by the IR camera that shows optical transmission after adding the iris to the image plane.

## 6. Results

Each VCSEP device can be represented as a series of Fabry-Pérot (FP) resonators, with three distinct resonators, as depicted in the VCSEP cross-section presented in Fig. 7. The first resonator comprises an air-silicon wafer-VCSEP arrangement, the second consists of an air-silicon wafer-air configuration, and the third resonator, which is our primary interest, features a silicon wafer-VCSEP-air composition.

Identifying the resonance response of each resonator is crucial for interpreting the results obtained from characterizing the single VCSEP device, as illustrated in Fig. 7. The measured transmission corresponds to the collective response of the three resonators as the optical spot size surpasses the diameter of an individual VCSEP device. In this case, the aperture of the iris in the image plane imposes a constraint on the spot size, with the smallest aperture measuring 1 mm. Additional information on the response of these resonators and their Free Spectral Ranges (FSRs) can be found in Figs. 7(b) and (c).

The theoretical response depicted in Figs. 7(b) and 7(c) yields the following observations: The transmission spectra of the air-silicon wafer-air and the air-silicon wafer-VCSEP configurations exhibit a Free Spectral Range (FSR) of approximately 1 nm (as indicated in Fig. 7(b)). Moreover, Fig. 7(c) shows that the transmission spectra of the silicon-VCSEP-Air configuration have an FSR of approximately 70 nm. An individual VCSEP with a fabricated height of 7.403 µm device was optically characterized utilizing a tunable laser source that could be tuned from 1520 nm to 1610 nm. The input power of the laser was set to 10 dBm. The optical responses of the device were investigated by focusing the laser light on two different areas of the substrate, one where no VCSEP device was present and the other where a device was present. The results of these optical measurements are shown in Fig. 8.

To observe the Fabry-Perot (FP) behavior of the VCSEP device and its characteristics, it is necessary to eliminate the effect of the power spectra of the light source and its impact on coupling

Optics EXPRESS

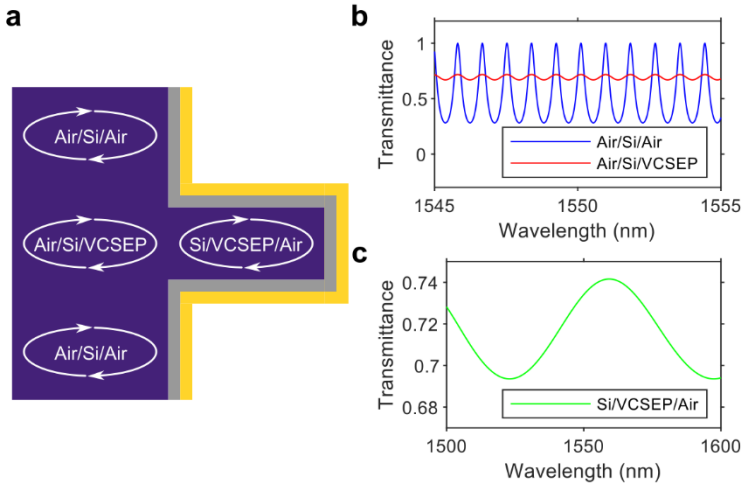


**Fig. 7.** A detailed cross-sectional theoretical model of the VCSEP device in three parts. Part (a) highlights the device's layered structure, comprising the highly doped silicon core, the nonlinear dielectric core (SRN), and the gold layer. Part (b) focuses on the theoretical optical response of the wafer resonator, which introduces high oscillation FP with a Free Spectral Range (FSR) of 1 nm and significantly impacts the device's overall performance. Part (c) demonstrates the combined effect of the wafer and the VCSEP device, offering insights into the device's optical behavior.

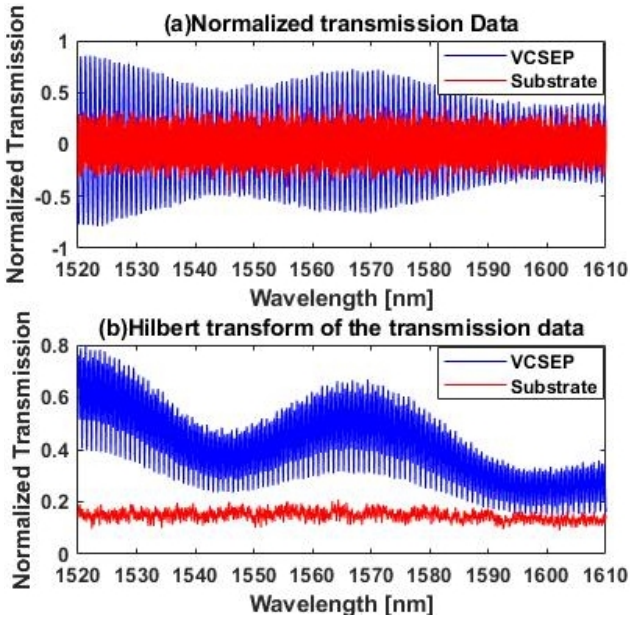


**Fig. 8.** The transmission spectrum of the VCSEP device and its corresponding silicon substrate can be represented by two distinct optical behaviors depicted by the blue and red curves, respectively: (a) shows the transmittance of the VCSEP device and substrate, normalized with respect to laser coupling efficiency; (b) The extraction of the Hilbert Transform of the transmission data, where the expected Free Spectral Range (FSR) of the VCSEP device is compared with the substrate response.

Optics EXPRESS

efficiency. This effect is normalized by dividing each measured transmission of the VCSEP device by its corresponding value of the laser transmission. The normalized data is shown in Fig. 8(a), where the normalized transmitted data. This standard normalization procedure enables a more precise characterization of the device's optical behavior by removing the influence of the laser source's varying coupling efficiency. The normalization procedure is applied to both data sets obtained from the substrate, with and without the VCSEP device present. The blue and red curves in the respective represent these data sets.

Next, a Hilbert Transform was applied to the transmission data obtained from the substrate and the VCSEP device to eliminate the rapid oscillations due to wafer resonance. This procedure resulted in a curve corresponding to the transmission of a single VCSEP device, represented by the blue line in Fig. 8(b). The Hilbert transform of the transmission data obtained from the substrate showed no slow oscillations. No VCSEP structure was present in those measurements. The optical response of an individual VCSEP device with an aspect ratio of 15 was estimated to have a Free Spectral Range (FSR) of $53.28 \pm 2.5$ nm, with transmission variation around 3 dB.

Figure 9 illustrates the electro-optic response of the VCSEP device. Figure 9(a) shows the wavelength shift as a function of applied voltage. Figure 9(b) illustrates the resulting changes in the effective index with the best fitting results as a function of applied voltage.

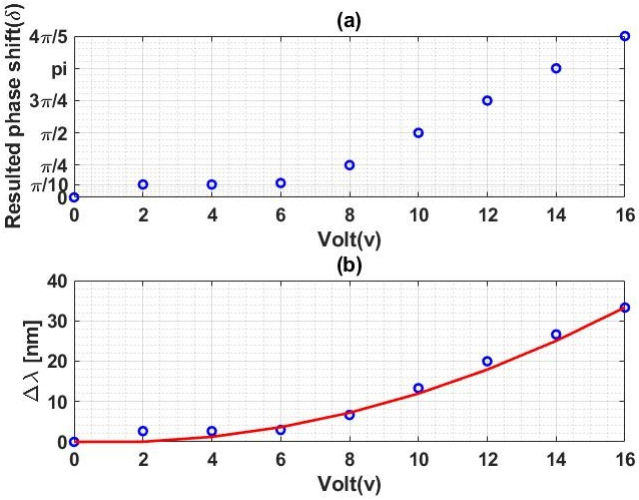


**Fig. 9.** The figure illustrates the electro-optic response of the VCSEP device, presenting two parts. Part (a) demonstrates the resulting phase shift (δ) in rad representation as a function of the applied electrical field Part (b) shows the wavelength shift in nanometer versus the applied electrical field.

This response quantitatively measures the device's phase-shifting capabilities, highlighting the relationship between the applied electrical field and the resulting phase shift. It is observed that a π phase shift can be introduced by applying a voltage equal to 14 V, which equals a shift in the wavelength to 53.28 nm. Moreover, we can estimate the value of VπL, equal to 0.0075 V-cm, and insertion loss equal to 69 dB. The VCSEP device demonstrates a maximum phase shift of 1.25π under an applied electric field intensity of 16 V. Furthermore, the variation in the effective index can be estimated using the equation below:

$$\frac{\Delta n}{n}\frac{L_{mod}}{L_{total}} = \frac{\Delta\lambda}{\lambda} \tag{1}$$

Using the developed COMSOL model of the VCSEP device, we can extrapolate the mode length ($L_{mod}$) and total interaction length ($L_{total}$) to estimate the variation in the effective index as

Optics EXPRESS

a function of applied voltage. A cavity finesse of 5 means that a photon makes 5 round trips through the cavity, resulting in an effective interaction length of 1.48 mm, which is 200x the free space interaction length. This is due to the combination of hybrid plasmonic localization and the low finesse cavity. The best fitting is achieved by using the following equation:

$$\Delta n = \frac{3\Gamma_{SRN}}{2} \times \frac{\chi^3}{n_g} E^2 + \frac{3\Gamma_{SRN}}{2} \times \frac{\chi^2}{n_g} E \tag{2}$$

Where $\Gamma_{SRN}$ is the mode overlap with SRN and E is the applied electric field across the VCSEP, From Eq. (2) we can estimate The best fitted Δn is 0.00052, but the measured value is 0.00452, with a difference of $9.5 \times 10^{-5}$.

## 7. Discussion

The results presented in this study demonstrate the effectiveness of the VCSEP device for optical applications. The device was characterized using a tunable laser, and the responses of its three distinct Fabry-Perot resonators were analyzed. The measurements yielded an FSR of 1 nm for the air-silicon wafer-air and air-silicon wafer-VCSEP configurations and an FSR of 70 nm for the silicon-VCSEP-Air configuration.

A normalization procedure was applied to the data obtained from the substrate to obtain a more accurate characterization of the device's optical behavior. A Hilbert Transform eliminated the rapid oscillations due to wafer resonance. The resulting analysis provided an estimated FSR of $53.25 \pm 2.5$ nm for the measured VCSEP Fabry-Perot, within the expected range, despite being off by approximately 16.75 nm from the module-suggested FSR of 70 nm. The discrepancy between the measured and estimated FSR values is due to variations in the thickness of the gold, SRN, and silicon pillars. These variations can arise from the deposition process, the SRN layer uniformity, and the etching precision. The overall thickness of the VCSEP device can vary, which affects the FSR.

According to simulation results, the VCSEP configuration was estimated to have an insertion loss of 2500 dB/cm. In theory, experimental verification of this value could be accomplished using the finesse of the resonator. However, accurately estimating the exact insertion loss of the VCSEP device is challenging due to its small size. The device is estimated to be less than 1 μm in dimension, and when considering the total magnification of the setup (100x), the imaged device appears to be less than 100 μm. This can be observed in Fig. 6(c), which indicates that the VCSEP occupies less than 50% of the image. Moreover, the presence of multiple resonances from the presence of multiple interfaces in the fabricated sample results in a complex experimental spectrum that renders this extraction impossible.

Considering the total experimental structure (not only the VCSEP but the substrate wafer, etc.) reveals several additional sources of optical loss. The measured insertion loss is 69 dB, which can be attributed to several factors. The most significant loss is due to the high absorption coefficient of the n-doped silicon wafer, which has a doping concentration of $4.5 \times 10^{18}\,\mathrm{cm}^{-1}$. This contributes to insertion losses of 50 dB. The gold layer and multiple reflections between the gold, SRN, and silicon layers also contribute to the optical loss. However, these losses are relatively small compared to the loss due to the doped silicon backing layer. One approach to improve the VCSEP device in the future is to thin the wafer to reduce the optical losses as a result of the high doping concentration.

The difference between the best fitting result from the Δn can be attributed to the non-ohmic contact. Non-ohmic contacts exhibit nonlinear current-voltage characteristics due to the high barrier height at the metal-semiconductor junction in non-ohmic contacts, which inhibits the flow of charge carriers across the junction. As a result, the voltage required to vary the effective index is higher.

Optics EXPRESS

Furthermore, the VCSEP device was found to have VπL equal to 0.0075 V-cm, equivalent to 0.075 V-mm. This value is comparable to typical P-i-n devices with a $V_\pi L$ of 0.036 V-mm [17]. In contrast, the typical Si modulator has a $V_\pi L$ of 2 to 3 V-cm [18]. The high $V_\pi L$ of our device is made possible by the combination of its vertical cylindrical topology, hybrid plasmonic guided modes, relatively high $r_{33}$ of SRN, and Fabry-Pérot resonance in the vertical direction of propagation. Furthermore, the device's performance can be further improved by utilizing a nonlinear material such as silicon-rich nitride (SRN), which has been shown to demonstrate a third-order nonlinear susceptibility, $\chi^{3}$, as high as $(6 \pm 0.58) \times 10^{-19}$ $m^2/V$ with an index equals to 3.01 [11].

One way to enhance the design is to use thermal annealing to reduce the Schottky barrier and establish an ohmic contact by forming a silicide layer at the metal-silicon interface. The choice of metal for the contact can vary depending on the type and concentration of doping. For n-doped silicon, such as in our case, platinum (Pt) is commonly used as the contact metal in the literature [19]. The sample can then be thermally annealed using Rapid Thermal Annealing (RTA) at a temperature range of 400°C to 500°C for 5 to 10 minutes, depending on the doping concentration. Higher doping concentrations require lower annealing temperatures and times [19].

This detailed analysis of the transmission spectrum of the VCSEP device and its comparison with the silicon substrate provides valuable insights into the device's optical properties and potential applications in photonic systems.

## 8. Conclusion

This manuscript introduces an innovative approach to developing compact phase shifters for LIDAR applications using hybrid resonance structures in a cylindrical topology. The study showcases fabricated devices with high aspect ratios and small footprints, enabling dense integration of VCSEPs. By applying normalization procedures and analysis techniques, the study accurately characterizes the optical behavior of the VCSEP device. Despite uncertainties in measuring insertion loss, the study demonstrates the promising potential for optical applications, with the VCSEP device having a $V_\pi L$ 0.075 V-mm comparable performance to state-of-the-art devices. The findings provide valuable insights into the optical properties of the VCSEP device and suggest future research directions in utilizing nonlinear materials for enhanced performance. Overall, the study paves the way for developing high-performance, compact electro-optic phase shifters suitable for various LIDAR applications.

**Funding.** Cymer (LEED); U.S. Department of Energy (DE-SC0019273); Army Research Office (ECCS-2025752); Office of Naval Research (ECCS-180789, NSF ECCS-190184, NSF ECCS-2023730); Defense Advanced Research Projects Agency (DSO NAC Programs).

**Acknowledgments.** The author, Dhaifallah Almutairi, would like to acknowledge the support provided by King Abdulaziz City for Science and Technology (KACST) during their study. The author also like to thank the DARPA Microsystem Technology Office (MTO) for their help and assistance throughout the project period. The authors also extend their appreciation to the nano3 cleanroom staff at UCSD and Dr. Maribel Montero for their valuable assistance in fabricating the samples. In addition, the author would like to express gratitude to the CPTF lab for granting access to their facilities for characterizing the demonstrated device.

**Disclosures.** The authors declare no conflicts of interest.

**Data availability.** Data underlying the results presented in this paper are not publicly available but may be obtained from the authors upon reasonable request.

## References

1. P.-C. Kuo, S.-I. Kuo, J.-W. Wang, Y.-H. Jian, Z. Ahmad, P.-H. Fu, Y.-C. Chang, J.-W. Shi, D.-W. Huang, Y. Liu, C.-H. Yeh, and C.-W. Chow, Actively Steerable Integrated Optical Phased Array (OPA) for Optical Wireless Communication (OWC); Actively Steerable Integrated Optical Phased Array (OPA) for Optical Wireless Communication (OWC) (2022).
2. C. V. Poulton, M. J. Byrd, P. Russo, E. Timurdogan, M. Khandaker, Di. Vermeulen, and M. R. Watts, "Long-Range LiDAR and Free-Space Data Communication with High-Performance Optical Phased Arrays," IEEE J. Sel. Top. Quantum Electron. **25**(5), 1–8 (2019).

Optics EXPRESS


3. Shengping Liu, Y. Tian, Y. Lu, and J. Feng, *Comparison of thermo-optic phase-shifters implemented on CUMEC silicon photonics platform*, in (SPIE-Intl Soc Optical Eng, 2021), p. 328.
4. A. F. Fercher, W. Drexler, C. K. Hitzenberger, and T. Lasser, "Optical Coherence Tomography-Principles and Applications," Rep. Prog. Phys. **66**(2), 239–303 (2003).
5. "Review on LiDAR Technology Srushti Neoge · Ninad Mehendale (n.d.),".
6. N. Li, C. P. Ho, J. Xue, L. W. Lim, G. Chen, Y. H. Fu, and L. Y. T. Lee, "A Progress Review on Solid-State LiDAR and Nanophotonics-Based LiDAR Sensors," Laser Photonics Rev. **16**(11), 1 (2022).
7. J. Sun, E. Timurdogan, A. Yaacobi, E. S. Hosseini, and M. R. Watts, "Large-scale nanophotonic phased array," Nature **493**(7431), 195–199 (2013).
8. B. Janjan, D. Fathi, M. Miri, and M. Ghaffari-Miab, "Ultra-wideband high-speed Mach–Zehnder switch based on hybrid plasmonic waveguides," Appl. Opt. **56**(6), 1717 (2017).
9. R. F. Oulton, V. J. Sorger, D. A. Genov, D. F. P. Pile, and X. Zhang, "A hybrid plasmonic waveguide for subwavelength confinement and long-range propagation," Nat. Photonics **2**(8), 496–500 (2008).
10. J. Wang, X. Guan, Y. He, Y. Shi, Z. Wang, S. He, P. Holmström, L. Wosinski, L. Thylen, and D. Dai, "Sub-Mm 2 Power Splitters by Using Silicon Hybrid Plasmonic Waveguides," Opt. Express **19**(2), 838–847 (2011).
11. A. Friedman, H. Nejadriahi, R. Sharma, and Y. Fainman, "Demonstration of the DC-Kerr effect in silicon-rich nitride," Opt. Lett. **46**(17), 4236 (2021).
12. S. Habermehl, R. T. Apodaca, and R. J. Kaplar, "On dielectric breakdown in silicon-rich silicon nitride thin films," Appl. Phys. Lett. **94**(1), 1 (2009).
13. D. K. T. Ng, Q. Wang, T. Wang, S. K. Ng, Y. T. Toh, K. P. Lim, Y. Yang, and D. T. H. Tan, "Exploring High Refractive Index Silicon-Rich Nitride Films by Low-Temperature Inductively Coupled Plasma Chemical Vapor Deposition and Applications for Integrated Waveguides," ACS Appl. Mater. Interfaces **7**(39), 21884–21889 (2015).
14. H.-H. Lin, R. Sharma, M.-H. Yang, M. W. Puckett, C. D. Wurm, F. Vallini, and Y. Fainman, "Enhanced Effective Second-Order Nonlinearities in Si-Rich SiN x Thin Films," (2017).
15. K. Grigoras, L. Sainiemi, J. Tiilikainen, A. Säynätjoki, V. M. Airaksinen, and S. Franssila, "Application of ultra-thin aluminum oxide etch mask made by atomic layer deposition technique," J. Phys.: Conf. Ser. **61**(1), 369–373 (2007).
16. Y.-J. Hung, S.-L. Lee, and L. A. Coldren, *et al.*, "DChallenges and Prospects of Nanopillar-Based Solar Cells," Nano Res. **2**(11), 829 (2009).
17. H. C. Nguyen, S. Hashimoto, and M. Shinkawa, *et al.*, "Ultra-Compact, Low RF Power, 10 Gb/s Silicon Mach-Zehnder Modulator," Opt. Express **15**(25), 17106 (2007).
18. H. C. Nguyen, S. Hashimoto, M. Shinkawa, and T. Baba, "Compact and fast photonic crystal silicon optical modulators," Opt. Express **20**(20), 22465–22474 (2012).
19. G. P. Lousberg, H. Y. Yu, B. Froment, E. Augendre, A. De Keersgieter, A. Lauwers, M. F. Li, P. Absil, M. Jurczak, and S. Biesemans, "Schottky-barrier height lowering by an increase of the substrate doping in PtSi Schottky barrier source/drain FETs," IEEE Electron Device Lett. **28**(2), 123–125 (2007).